Smart Compression Stockings Driven by Interpretable Unsupervised Deep Learning

Heng Luo, *Student Member, IEEE,* Ying Xiong, Shuo Wang, and Xiaoming Tao, *Member, IEEE*

***Abstract*— Accurate, real-time pressure monitoring is critical for the effective management of chronic venous disease, necessitating advanced solutions in compression therapy. This study presents a novel smart compression stocking system that integrates cost-effective, laboratory-fabricated textile capacitive pressure sensors within compression garments, a compact edge control unit, a dedicated mobile application, and advanced edge signal processing algorithms. Although simply fabricated textile-based sensors are highly sensitive and scalable, their accuracy can be affected by parasitic capacitance, electromagnetic interference, proximity effects, and deformation on curved surfaces. To address these challenges, we developed a physics-informed encoder–decoder deep neural network architecture that enhances noise reduction and enables high-resolution pressure detection. The encoder, constructed from the symmetrical stacked autoencoder, performs nonlinear feature extraction and incorporates soft physical constraints, while the decoders are tailored for specific downstream tasks. This lightweight, interpretable architecture is computationally efficient and suitable for deployment on resource-constrained edge devices. Empirical validation was conducted using representative datasets, comprising 22,498 capacitance–pressure data pairs from 100-minute flat surface pressure recordings and 75,888 pairs from 12-minute curved surface pressure recordings over ten days. The proposed algorithms achieved a root mean square error (RMSE) of 0.7891 mmHg for flat surfaces, a 38% improvement over polynomial regression, and RMSEs of 0.0283 mmHg, 0.0633 mmHg, and 0.0387 mmHg at curved surface positions B, B1, and C, representing improvements of 98%, 97%, and 98%, respectively. These results demonstrate the system's potential to deliver precise, real-time, accessible, and scalable pressure monitoring, marking a significant advancement in the conservative management of chronic venous disease.**

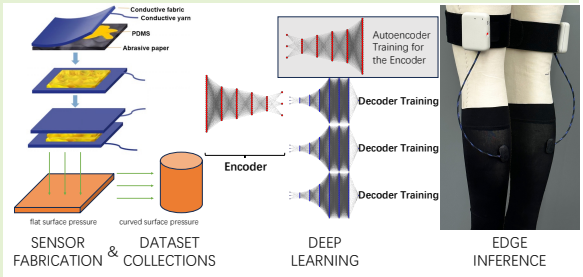

***Index Terms*— Integrated smart compression stocking system, unsupervised deep learning, interpretable deep learning.**

I. Introduction

CHRONIC Venous Disease (CVD), also known as Chronic Venous Insufficiency (CVI), is a widespread and debilitating vascular disorder characterized by impaired venous return and blood pooling in the lower extremities. Epidemiological data indicate a prevalence of 60–70% [1], with significant health impacts affecting 5% to 30% of adults globally [2].

Compression therapy remains the cornerstone of conservative management for venous insufficiency, owing to its efficacy and minimal side effects. This therapeutic approach involves the external application of graduated pressure, typically via medical compression stockings (MCSs) or bandages, to counteract abnormal venous pressure distributions. The pressure gradient, highest at the ankle and decreasing proximally, facilitates venous return, reduces venous hypertension and wall distension, restores valve function, and improves both hemodynamic and lymphatic circulation. Consequently, compression therapy alleviates symptoms such as swelling and edema and may reduce inflammation. For optimal outcomes, the selection of compression level is tailored to disease severity: mild cases benefit from 10–20 mmHg, varicose veins from 20–30 mmHg, active ulcers from 30–40 mmHg, and severe conditions such as lymphedema may require 40–50 mmHg or higher [3]. However, both insufficient and excessive compression can be ineffective or even detrimental [4], underscoring the need for precise pressure control. Long-term, continuous use of MCSs, typically for at least four to six months, is recommended, with exceptions only for bathing and sleeping.

Despite the clinical benefits of compression therapy, current solutions lack the capability for accurate, real-time pressure monitoring, revealing a significant gap in both clinical practice and research. Although various sensor technologies, including piezoresistive [5]–[8], resistive stretch [9], optical fiber [10], [11], and capacitive pressure sensors [12]–[14], have been explored, there remains a lack of comprehensive frameworks that integrate hardware, software, and advanced algorithms for smart compression systems across diverse clinical scenarios.

This research was funded by the Innovation and Technology Commission of the Hong Kong SAR Government, under grant number ITT/011/23TP. This work involved human subjects or animals in its research. Approval of all ethical and experimental procedures and protocols was granted by the Hong Kong Polytechnic University Institutional Review Board, under Application No. HSEARS20230717004.

Heng Luo, Ying Xiong, Shuo Wang, and Xiaoming Tao are with the Research Institute for Intelligent Wearable Systems and the School of Fashion and Textiles, Hong Kong Polytechnic University, Hong Kong, SAR. (e-mail: henryheng.luo@connect.polyu.hk, ying-xy.xiong@connect.polyu.hk, 22037796r@connect.polyu.hk, xiaoming.tao@polyu.edu.hk).

The rapid development of flexible textile sensors has outpaced advances in robust signal processing methods necessary to optimize their performance. These sensors are inherently susceptible to electromagnetic interference, proximity effects, and mechanical deformation, particularly on curved anatomical surfaces, which compromises their sensitivity, stability, and reliability [15], [16]. The resulting weak signals, often in the micro- to pico-scale range, require amplification and complex circuitry, which can introduce additional noise and further degrade signal quality.

Signal processing for sensor calibration and denoising presents additional challenges. Traditional techniques, such as frequency-domain and adaptive filtering, including Wiener, least mean square (LMS), recursive least square (RLS), and Kalman filters, are widely used due to their maturity and interpretability. While effective at removing noise within specific frequency bands, these methods are fundamentally limited by their reliance on prior knowledge of noise characteristics and their inability to address the non-stationary, nonlinear, and overlapping noise sources typical in wearable sensor applications [17], [18]. Furthermore, acquiring well-defined reference signals for adaptive filtering is difficult, and these methods are sensitive to initial parameter settings, which can lead to suboptimal performance or divergence.

Advanced signal processing methods, such as adaptive denoising with reference noise generators [19], [20], wavelet transforms [21]–[23], and empirical mode decomposition (EMD) [24], [25] offer improved handling of non-stationary noise but introduce significant computational complexity and risk of information loss. The selection of optimal wavelet basis functions, the computational burden of extracting intrinsic mode functions, and the potential for over-decomposition or mode mixing further complicate their application.

These multifaceted issues give rise to three central research questions: How can pressure monitoring in compression therapy be made more accurate, accessible, and scalable? What methods can overcome the inherent limitations of potential flexible sensors, such as manual calibration, susceptibility to noise and deformation on curved surfaces? How can novel signal processing be leveraged to ensure robust, real-time performance on resource-constrained edge devices?

To address these pressing challenges, this study advances the field through three primary contributions.

(1) We introduce a novel smart compression stocking system that integrates cost-effective, laboratory-fabricated textile capacitive pressure sensors within compression garments, a compact edge control unit, a dedicated mobile application, and advanced edge signal processing algorithms. This integrated system is designed to deliver accurate, real-time pressure monitoring, thus enhancing both the effectiveness and accessibility of compression therapy.

(2) Recognizing the susceptibility of low-cost textile sensors to parasitic capacitance, electromagnetic interference, proximity effects, and deformation on curved anatomical surfaces, we developed an automated, data-driven calibration framework. Leveraging a unified encoder–decoder deep neural network architecture, this approach enables the model to learn complex sensor behaviors from representative datasets and generalize calibration across diverse scenarios, achieving high-resolution, noise-robust pressure detection on both flat and curved surfaces without the need for labor-intensive, device-specific calibration.

(3) To ensure interpretability, physical plausibility, and computational efficiency for deployment on edge devices, our encoder–decoder multilayer perceptron architecture incorporates soft physical constraints within the encoder, constructed from the symmetrical stacked autoencoder for effective nonlinear feature extraction. The decoders are tailored for specific downstream tasks, maintaining model interpretability and efficiency. We further investigate optimal architectural design, including model depth, width, initialization, and fine-tuning strategies, to ensure robust generalization and reliable performance across a range of sensing conditions.

The remainder of this paper is organized as follows. Section 2 presents the design and implementation of a novel smart compression stocking system that integrates compression garments with embedded fabric pressure sensors, a compact edge control unit, a dedicated mobile application, and advanced edge signal processing algorithms. Section 3 details the development and empirical validation of a physics-informed encoder–decoder deep neural network architecture. Section 4 discusses the training, testing, and performance evaluation of the proposed algorithms, followed by the study's conclusions in Section 5.

II. System design

The present study investigated an integrated system for smart compression stockings. The system was designed to capitalize on both static and dynamic pressure responses, offering high pressure sensitivity, commendable accuracy, flexibility, and user-friendliness. The architectural pipeline of the system is illustrated in Fig. 1.

The laboratory-fabricated textile capacitive pressure sensors, featuring a sandwich structure, provide several benefits: straightforward fabrication, satisfactory accuracy and repeatability, high sensitivity particularly in the low-pressure range below 50 mmHg, low energy consumption, and prompt response times. These flexible sensors are placed at the B point, B1 point, and C point on the compression stocking, in alignment with the RAL-GZ 387/1 standard [26], which is the German standard for quality assurance in medical compression hosiery.

The edge control unit, noted for its cost-effectiveness and low power requirements, is tasked with the detection, processing, and wireless transmission of electrical signals. To complement the system, an Android mobile application was developed, offering data visualization capabilities and an intuitive user interface, thereby enhancing user interaction with smart compression stockings. Edge signal processing algorithms are suitably deployed on the edge control units or users' mobile phones to achieve high-resolution pressure detection.

A. Fabric sensors material and fabrication

Static pressure measurement should cover the range of 0 to 50 mmHg [27]. Dynamic pressure is involved, considering

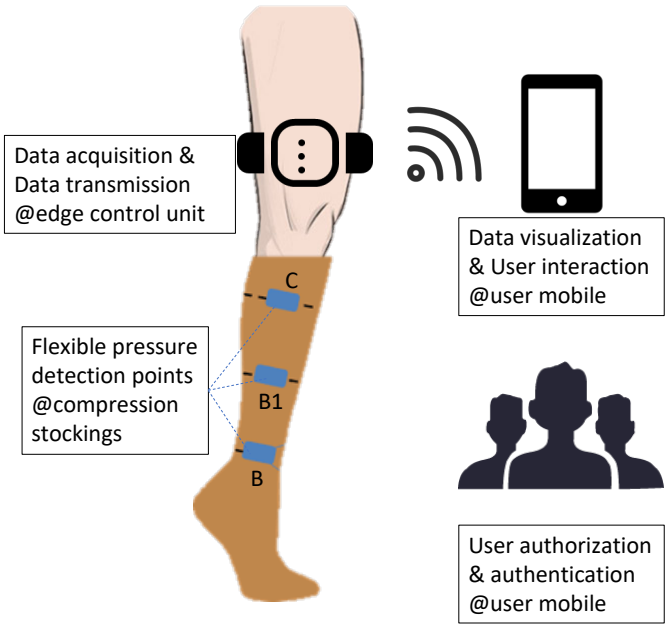

Fig. 1. Architecture pipeline design for the integrated smart compression stocking system, including compression garments, embedded fabric pressure sensors, an edge control unit, a user mobile application, and edge signal processing algorithms.

the users' activities and exercises. Relatively high sensitivity in the low-pressure range below 50 mmHg, stable continuous output, resilience to temperature impact and humidity impact, small size and thinness, high flexibility, and conformation on the curved surface are all desired characteristics.

Consequently, the adoption of cost-effective fabric capacitive pressure sensors was deemed appropriate. The sensor's design incorporated a sandwich structure, which entailed the use of two conductive fabric layers functioning as electrodes, separated by a dielectric layer. This dielectric layer was fabricated from a composite of polydimethylsiloxane (PDMS) and carbon black (CB) powder, and subsequently processed with abrasive paper to enhance its properties. To augment their durability and resistance to external friction and strain, the sensors were encased in thermoplastic polyurethane (TPU) protective layers. These flexible capacitive pressure sensors are designed to be affixed to various points on compression stockings.

The performance of the flexible sensors underwent rigorous evaluation, encompassing tests for sensitivity, hysteresis, and repeatability. The initial capacitance measured in the absence of external load was approximately 17 pF. As illustrated in Fig. 2(b), the sensors demonstrated a sensitivity of 3.44 kPa^{-1} within the 0–0.2 kPa pressure range, 0.38 kPa^{-1} in the 0.2–2 kPa range, and 0.19 kPa^{-1} in the 2–9 kPa range. Hysteresis was quantified at approximately 8% at a pressure of 4 kPa, as shown in Fig. 2(c). Furthermore, the sensors exhibited excellent repeatability, maintaining stable capacitance responses throughout 10,000 loading cycles, as depicted in Fig. 2(d).

B. Edge control unit design and mobile application design

The edge control unit was designed with a focus on safety, low power consumption, cost-effectiveness, sustainability, and portability. To meet these requirements, the unit was constructed using commercially available components. The system is centered around an STM32 microcontroller (STMicroelectronics, Geneva, Switzerland), with a PCap01 (Sciosense B.V., Eindhoven, The Netherlands) as the capacitance analog-to-digital converter. Bluetooth Low Energy (BLE) connectivity is provided by the nRF51802 processor (Nordic Semiconductor, Trondheim, Norway), while charging is managed by the TP4059 chip (Top Power ASIC Corp., Nanjing, China). The device is powered by a 2400 mAh lithium battery, supporting up to 8 hours of continuous operation for three consecutive days. The total bill of materials is approximately US$33 [28].

The STM32 microcontroller handles both power management and data transmission. Capacitance data from the PCap01 is transferred via Serial Peripheral Interface (SPI) to the STM32, and then relayed to the nRF51802, which transmits the data wirelessly to user smartphones via BLE. The TP4059 chip enables USB charging, with LED indicators showing charging status. The hardware is assembled on a compact 63 × 45 mm two-layer printed circuit board (PCB), chosen for its efficiency and resistance to interference. The enclosure, produced by 3D printing, features chamfered edges to enhance user safety, as shown in Fig. 3.

Commercial smartphones act as the main user interface, offering information display, alerts, notifications, and recommendations. Data from the edge control unit is stored in an SQLite database on the smartphone, which also performs major computational tasks, reducing the processing and power burden on the edge device.

To support widespread Android use, the "Smart Compression Stocking Utility version 1" application was developed for Android 8.0 and above. The app utilizes Android's architecture, Bluetooth protocol, socket methods, and native binder to ensure stable communication. It supports user login, Bluetooth device scanning and pairing, and real-time data visualization in graphical, textual, and analytical formats, as illustrated in Fig. 4.

C. Encoder-decoder-based edge signal processing design

For the smart compression stocking system, the signal processing's purpose is to spontaneously calculate corresponding pressure values based on measured sensors' capacitance values. The tasks should be implemented on the edge control units or users' mobile phones. Therefore, limited computation and storage resources constrain desired algorithms.

The encoder-decoder architecture has garnered significant research interest for its applicability in unsupervised learning, sequence-to-sequence tasks, and its enhanced interpretability and rapid module adaptation. This architecture comprises two main components: the encoder, which converts a variable-length input sequence into a fixed-dimensional state representation, and the decoder, which reconstructs a variable-

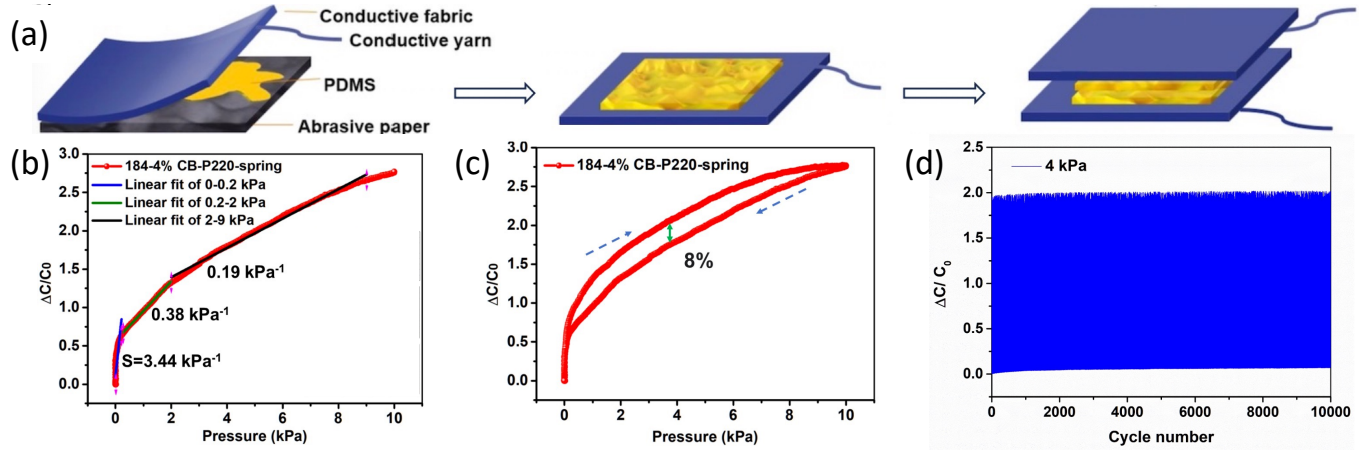

Fig. 2. Fabrication and performance of fabric capacitive pressure sensors [37]. (a) Fabrication process. (b) Sensitivity testing. (c) Hysteresis testing. (d) Repeatability testing.

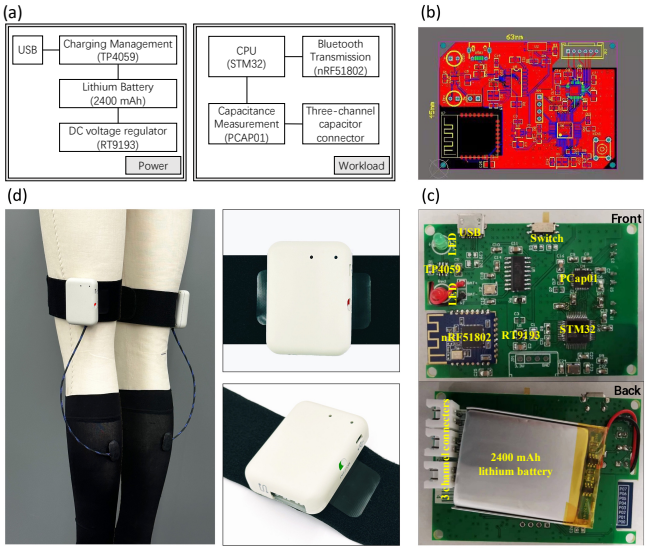

Fig. 3. Illustrations of the edge control unit design. (a) Schematic diagram of the edge control unit design. (b) PCB layout diagram. (c) Circuit assembly prototypes. (d) Housing design and connected edge control unit prototypes.

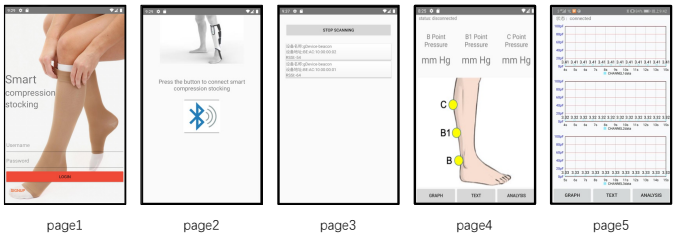

Fig. 4. Illustrations of the Smart Compression Stocking Utility. User experience flows from logging in, scanning and finding Bluetooth devices, pairing with desired devices, and data visualization.

length sequence from the encoded state or the codings [29]. Both components are modular and can be interchanged with alternative encoders or decoders through fine-tuning.

Calculating pressure from measured capacitance in flexible pressure capacitive sensors is not straightforward due to their complex properties, including nonlinear response, background noise, viscosity, and hysteresis. The conventional methodology employs the parallel plate capacitor model to describe.

$$C = \frac{\varepsilon A}{d} \tag{1}$$

where C is the capacitance value, A is the contact area of two parallel conductive plates, d is the distance between the two plates, and ε is the permittivity of the dielectric filled into space between the two plates. As the pressure P is exerted on the flexible sensor, ε, A, and d will change accordingly. Therefore, to obtain the pressure theoretically involves two principal mechanisms: one is to map the C space to the ε, A, d spaces, and the other is to map the ε, A, d spaces to the P space. Given that any function can be accurately approximated by a neural network [30], these mechanisms can be represented by two Multilayer Perceptron (MLP). One MLP is named the encoder, whose task is to map input data (the C space) to codings (the implicit or explicit ε, A, d spaces), while the other MLP is named the decoder, whose task is to map the codings to output data (the P space). The training and development of the unified encoder-decoder MLP architecture followed a structured, four-phase process, as illustrated in Fig. 5.

III. Algorithms and Experiments Design

A. Autoencoder design

It is difficult to directly derive a close expression to map capacitance values to permittivity, contact area, and distance values. One alternatively feasible solution is to utilize machine learning to automatically extract deep features of capacitance values. The deep features can be regarded as latent representatives of desired permittivity, contact area, and distance values. Furthermore, to largely reduce data annotation, autoencoders were adopted as unsupervised learning considering the input and output of autoencoders are the same raw capacitance data during training and these raw capacitance data can be easily collected under different situations, such as various pressures, wearing on human legs, human movement.

The smart compression stocking system can measure the capacitance of flexible sensors with a sampling interval of

Procedure	Phase 1 Autoencoder Training&Testing	Phase 2 Encoder Inference	Phase 3 Decoder Training&Testing	Phase 4 Encoder-Decoder Inference
Model	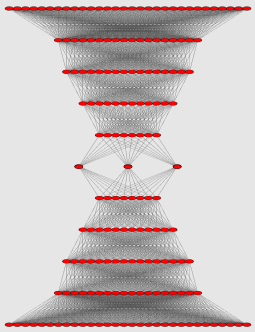	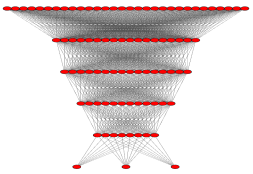	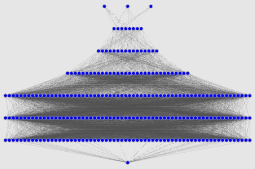	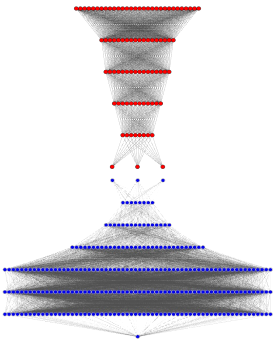
Data	**Dataset of Capacitance** all time-series capacitance values are segmented into groups of 30 consecutive data sequence		**Dataset of Capacitance-Pressure** capacitance values are preprocessed by encoder inference; training subset (80%) and testing subset (20%)	
Input	30 time-series capacitance values	30 time-series capacitance values	30 time-series capacitance values codings (intermediary data)	30 time-series capacitance values
Output	30 time-series capacitance values (the same sequence)	codings (ε, A, d)	the pressure value	the pressure value
Key Points	symmetrical stacked autoencoder with hyperbolic tangent activation functions; MSE loss with the regularization term; SGD optimizer with the learning rate of 0.001	freeze the first half of the trained autoencoder; hyperbolic tangent activation function optionally replaced by $x - x^3/3$	MLP with ReLU activation functions; MSE loss; SGD optimizer with the learning rate of 0.001; multiple decoders training	freeze the decoder; ReLU activation function optionally replaced by a comparator

Fig. 5. Four-phase training and development workflow of the unified encoder–decoder MLP architecture.

2s. To attain robust autoencoders against background noise and interference, a time series sequence of 30 elements was constructed as input data. The sequence stands for one-minute measure data. All of the input data was normalized to achieve zero-centered and ranging from -1 to 1 so that autoencoders can converge at a small number of iterations. Reversely, the output data could be denormalized to compare with the raw ground truth data.

To cut down the computation load, a typical architecture of the autoencoder is stacked by fully connected layers, with gradually decreasing encoder part neurons layer by layer until the codings layer, and symmetrical regarding the central codings layer, which exhibits a sandwich structure, as shown in Fig. 6. It has a mathematical representation of FC(30,18), FC(18,16), FC(16,12), FC(12,8), FC(8,3), FC(3,8), FC(8,12), FC(12,16), FC(16,18), FC(18,30), as defined in Equation (2).

$$y = f\left(Wx + B\right) \tag{2}$$

where $y \in R^{output}$, $x \in R^{input}$, $W \in R^{output} \times R^{input}$, $B \in R^{output}$, W and B are learnable matrices, $f(*)$ is the activation function of hyperbolic tangent function, which can be approximated using its Taylor expansion, as $x - x^3/3$. This reduces computational complexity, thus making it more feasible for real-time inference on edge control units. Hence the fully connected layer is written as FC(input,output). .

Machine learning, as a purely data-driven approach, faces inherent limitations. Firstly, without explicit physical constraints, models may yield predictions that violate fundamental laws of physics, resulting in implausible or physically unjustified outcomes. Secondly, their generalization ability is often restricted, hindering accurate predictions for untrained variables or unseen scenarios with different data distributions. Thirdly, the lack of interpretability and causal reasoning compromises reliability and trust. To overcome these challenges, incorporating physical laws into machine learning has become an effective strategy. This integration combines the predictive power of data-driven models with the rigor of physics-based reasoning, improving accuracy, interpretability, and generalization. Four primary paradigms have emerged, distinguished by the stage at which physical knowledge is embedded [31]. Among these, physics-informed machine learning incorporates governing physical equations as penalty terms within the loss function, thereby ensuring that model predictions adhere to established physical laws during training. This approach is widely adopted as a form of soft constraint due to its straightforward implementation and interpretability. In the study, the autoencoder was trained using a loss function composed of the Mean Squared Error (MSE) combined with an L2 regularization term, as shown in Equation (3). The regularization term serves to constrain the codings energy. Unlike L1 regularization, which can drive some coefficients to exactly zero and thus promote sparsity, L2 regularization uniformly shrinks all coefficients towards zero without eliminating them entirely. This encourages a balanced contribution from each feature and reduces the likelihood that any single feature will dominate the model. Therefore, the loss function implicitly implies physical relationships, such that changes in the ε, A, d are reflected in response to applied pressure P on the flexible sensor.

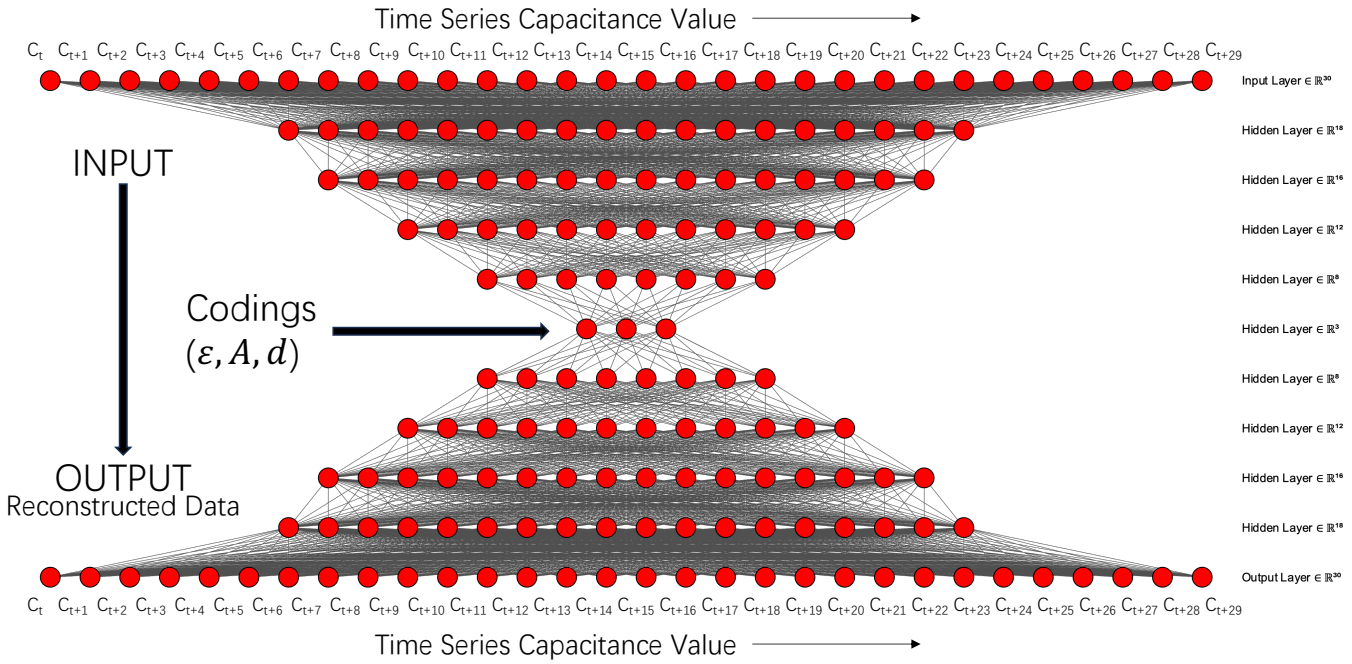

Fig. 6. One typical autoencoder structure.

$$Loss = \frac{\sum_{i=0}^{n}(y_i - \hat{y}_i)^2}{n} + \lambda \sum_{i=0}^{m}(coding_i)^2 \tag{3}$$

where y_i is the output of the autoencoder. $\hat{y}_i$ is the corresponding normalized ground truth value. n is the number of the sample size, setting $n = 30$. $coding_i$ is the codings of the autoencoder. m is the codings dimensionality, setting $m = 3$. λ is the weight ratio that determines the penalty impact of codings energy, empirically setting $\lambda = 0.0001$.

B. Decoder design

Similarly, MLPs were chosen as decoders containing sequential fully connected layers. As the typical codings of the autoencoder are of three dimensions, which means $coding \in R^3$, the input of the decoder is a three-dimensional vector. A typical decoder contains FC(3,8), FC(8,16), FC(16,32), FC(32,64), FC(64,64), FC(64,64), FC(64,1), as depicted in Fig. 7, whereas the activation function for the decoder was determined as Rectified Linear Unit (ReLU), which can be efficiently realized as a comparator in hardware implementations when deployed on edge control units with limited computational resources.

C. Flat surface pressure experiment design

The smart compression stocking, incorporating a randomly selected flexible textile capacitive sensor from the batch of laboratory-fabricated devices, was securely affixed to a flat, rigid surface to ensure uniform contact and eliminate confounding variables related to curvature or surface irregularities. Standard normal weights (Calibration Class F1 Weight Sets(1mg-100g), Shenzhen STX Electronic Technology Co., Ltd., China), including 0 g, 1 g, 2 g, 5 g, 10 g, 20 g, and 50 g were sequentially applied directly atop the sensor, and corresponding pressures were recorded by

$$P = \frac{MG}{S} \tag{4}$$

where M is the mass of the standard normal weight, $G = 9.8\ N/Kg$ is the acceleration of gravity, S is the contact area, and P is the exerted pressure. For each constant standard normal weight, continuous data readout for 100 minutes was recorded, considering the data fluctuation for a period. Therefore, the whole dataset consisted of 22,498 pairs (capacitance vs pressure) of data, as depicted in Fig. 8.

D. Curved surface pressure experiment design

To apply the flexible capacitive pressure sensors to human bodies, where conformable contact is achieved, it is important to do calibration on curved surfaces. The calibration experiment, as shown in Fig. 9, was designed as the following. Firstly one medium-sized wooden mannequin leg was adopted as a surrogate for the human limb. Secondly, a flexible sensor, randomly selected from the batch, was sequentially affixed to three anatomically representative positions on the mannequin leg: position B (circumference diameter 72 mm), position B1 (diameter 91 mm), and position C (diameter 115 mm). Thirdly, one standard sphygmomanometer cuff (type A mercury sphygmomanometer, Jiangsu Yuyue Medical Equipment & Supply Co., Ltd., China) was used to tightly wrap the sensor on the leg and to exert different pressure levels, including no pressure, 10 mmHg, 20 mmHg, 30 mmHg, 40 mmHg, 50 mmHg, and 60 mmHg pressure respectively. Fourthly, under each pressure level and each position, the capacitance values are recorded for continuous 12 minutes. Fifthly, the experiments

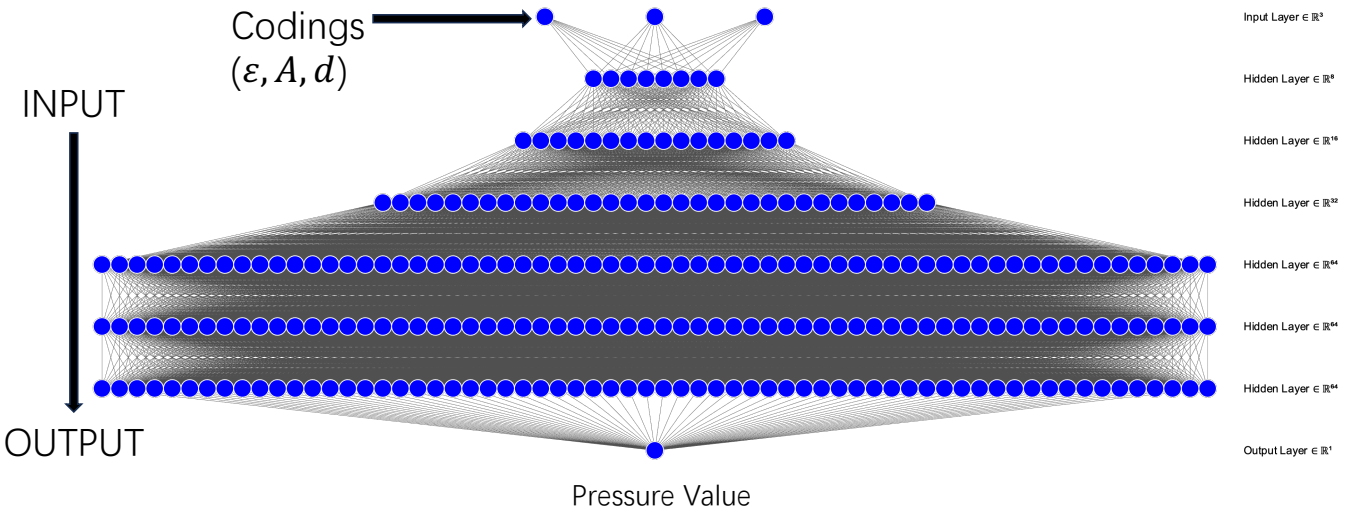

Fig. 7. One typical decoder structure.

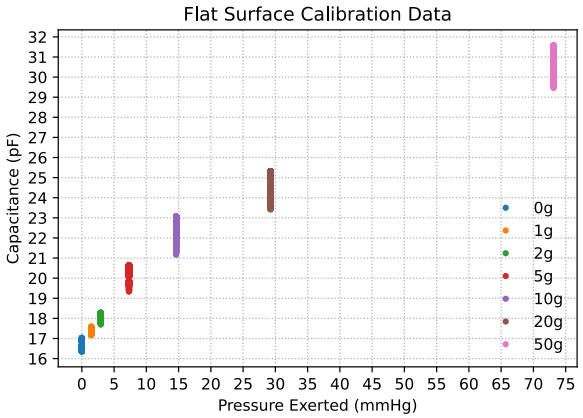

Fig. 8. Data distribution of the flat surface pressure dataset.

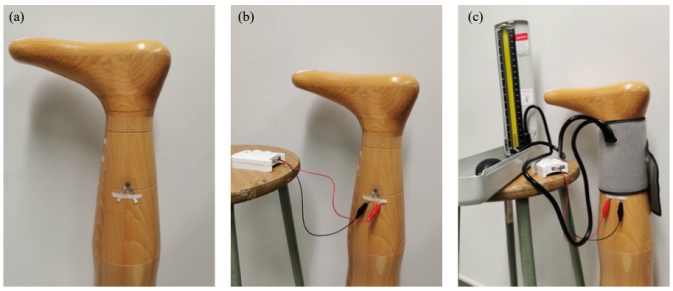

Fig. 9. Curved surface experiment procedures (for the B1 position).

were independently conducted for consecutive 10 days. Hence, the whole dataset of 75,888 pairs (capacitance vs pressure) was collected.

To visualize the dataset distribution of curved surface pressure, under each pressure level and each position in a day, the average capacitance value was calculated. The final different curved surface data distributions along the timeline were plotted in Fig. 10, Fig. 11, and Fig. 12. There are intuitive findings. Firstly, without pressure exerted, the initial

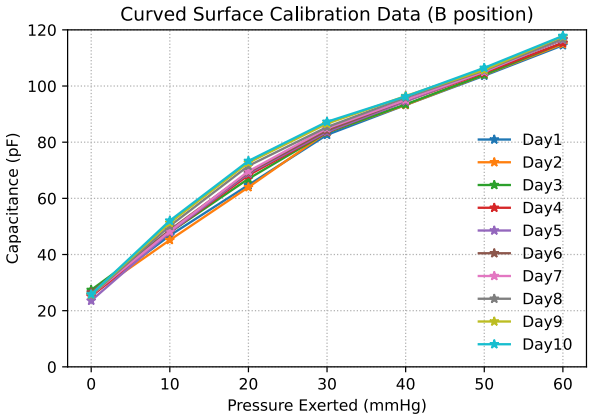

Fig. 10. Curved surface pressure data distribution (B position).

capacitance value remains approximately 20 pF for different curvature surfaces. Secondly, under the same pressure exerted and on the same curvature surface, the capacitance values have little fluctuation and keep a good consistency for 10 days. Thirdly, under the same pressure exerted, different curvature surfaces lead to different sensitivities. The higher curvature induces higher sensitivity.

E. Training and testing

Fig. 5 illustrates four-phase training and development workflow. In the initial phase, the focus was on extracting meaningful representations from the raw sensor data by training an autoencoder. Only capacitance values from the collected capacitance–pressure datasets were used and segmented into sequences of 30 consecutive capacitance readings, each corresponding to a one-minute measurement interval. These time-series segments served as input for training a symmetrical stacked autoencoder, which were tasked with learning nonlinear features and high-level abstractions from the sensor signals. The autoencoders were optimized using a MSE loss

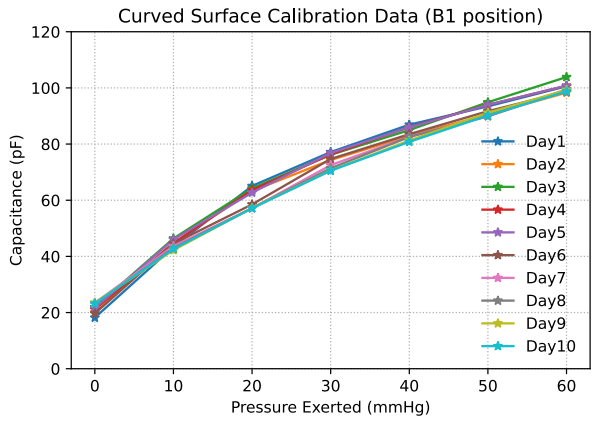

Fig. 11. Curved surface pressure data distribution (B1 position).

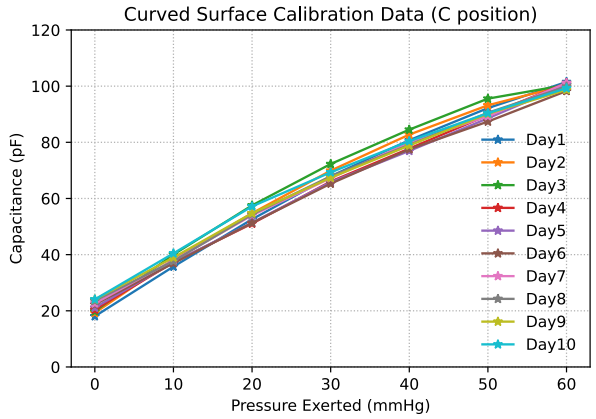

Fig. 12. Curved surface pressure data distribution (C position).

function augmented with a regularization term, as defined in Equation (3), and trained using Stochastic Gradient Descent (SGD) with a learning rate of 0.001. To ensure convergence and stability, training was conducted for 400,000 epochs. Model performance was evaluated by calculating the root mean square error (RMSE) between the denormalized autoencoder outputs and the ground truth capacitance values across the entire dataset.

$$RMSE = \sqrt{\frac{1}{t}\sum_{i=0}^{t}(y_i - \hat{y}_i)^2} \tag{5}$$

where $t = 22,498$ is the total number of the whole dataset, y_i is the denormalized output of the autoencoder, $\hat{y}_i$ is the corresponding ground truth value in the dataset.

In the second phase, the encoder component was derived by freezing the first half of the trained autoencoder. This encoder was responsible for transforming each 30-point capacitance sequence into a compact latent representation, denoted as codings(ε, A, d), which encapsulated the essential features required for subsequent pressure estimation.

The third phase involved the integration of the encoder with a decoder MLP for pressure prediction. The capacitance–pressure dataset was randomly partitioned into training

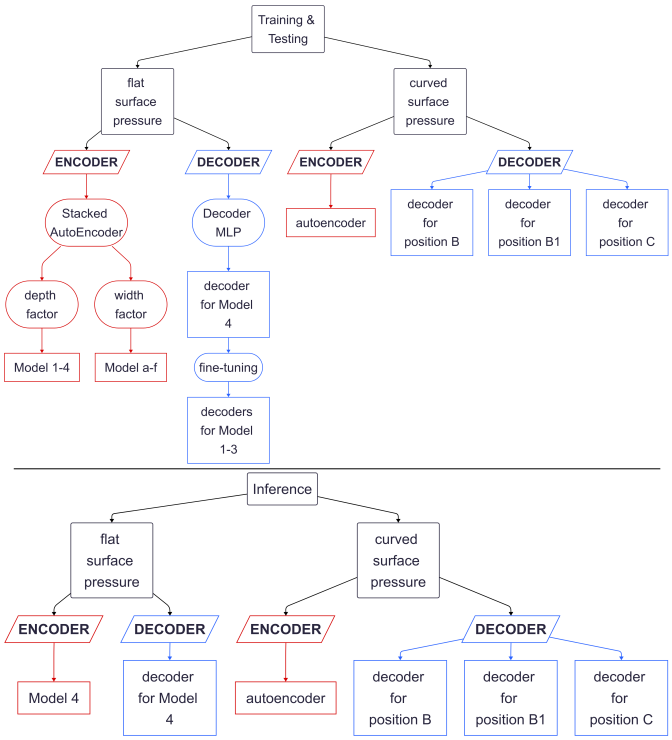

Fig. 13. Flowchart illustration of models training, testing and inference.

(80%) and testing (20%) subsets. The encoder was applied to the raw capacitance sequences to generate latent codings, which were then paired with the corresponding pressure values to form the input-output pairs for decoder training. The decoder was trained using the MSE loss and SGD optimizer, also for 400,000 epochs. To benchmark the proposed approach, polynomial regression methods of orders one through five were implemented as baselines, with parameters estimated via least squares on the training data. Model performance was assessed by computing the RMSE between the denormalized outputs and the ground truth pressure values in the testing subset, enabling a direct comparison between the proposed encoder-decoder MLP model and traditional regression methods. Significantly, multiple decoders may be trained for various tasks.

In the final phase, the decoder was frozen, resulting in a fully trained encoder–decoder MLP model suitable for inference and deployment on edge devices.

To systematically address the critical research challenges, a series of experiments were designed to evaluate the influence of model depth and width on autoencoder performance, assess decoder accuracy for flat surface pressure, investigate initialization strategies and fine-tuning protocols with different encoder substitutions, and examine the generalization capacity of the model for pressure estimation on curved surfaces with various curvatures. The overall workflow for model training, testing, and inference is summarized in Fig. 13.

1) The autoencoder depth factor: The influence of model depth on autoencoder performance for flat surface pressure was evaluated by training autoencoders (Model 1, Model 2, Model 3, and Model 4), as defined in Table I, with varying numbers of layers (4, 6, 8, and 10), using identical data segmentation

and optimization protocols, as illustrated in the Phase 1. This allowed for a rigorous assessment of how increasing model depth affected the extraction of relevant features from the capacitance data.

2) The autoencoder width factor: The effect of model width, defined as the dimensionality of the latent coding layer, was investigated. Autoencoders (Models a through f), as defined in Table II, with four fully connected layers were constructed, and the size of the coding layer was systematically varied from 1 to 6, while all other architectural and training parameters were held constant. This experiment provided insights into the impact of latent space dimensionality on the model's capacity to capture salient latent features from the capacitance data.

3) The decoder performance: Subsequent experiments focused on the decoder's predictive performance for flat surface pressure. The encoder from the deepest autoencoder (Model 4 with 10 layers) was frozen, and its latent codings were used as input to train the decoder. The decoder was trained and evaluated using the same protocols, as illustrated in the Phase 3, and its performance was directly compared to that of polynomial regression methods, providing a robust benchmark for the decoder's pressure prediction accuracy.

4) The fine-tuning performance: To further evaluate the robustness and adaptability of the decoder, fine-tuning experiments were performed. The decoder's parameters, initialized from the previously trained decoder model, were fine-tuned using frozen encoders from shallower autoencoder models (Model 1, 2 and 3 with 4, 6, and 8 layers respectively). Fine-tuning was conducted using SGD with an increased learning rate of 0.1 for 1,000 epochs. This protocol assessed the decoder's ability to accommodate variations in feature extraction strategies and initialization, reflecting real-world scenarios where sensor characteristics may differ across batches.

5) The generalization capacity: The generalization capacity of the proposed architecture was rigorously tested on curved surface pressure datasets, which present additional challenges due to varying sensor placements and geometric conformity. For each position (B, B1, and C), the same experimental workflow was applied: the autoencoder was trained on all time-series capacitance values, and then the dataset was split into training and testing subsets. Separate decoders were trained and evaluated for each position, with polynomial regression methods serving as comparative baselines. This comprehensive approach ensured that the model's performance and generalization were validated across diverse sensing scenarios, directly addressing the practical challenges of large-scale deployment and real-world variability in wearable sensor systems.

IV. Experimental Results and Discussion

A. Autoencoder experimental results for flat surface pressure

The performances of different number of layers for autoencoders are summarized in Table I and Fig. 14. There are some interesting findings. Firstly, as the model becomes deeper, the corresponding RMSE goes down dramatically, indicating better accuracy for data reconstruction. This verifies the deeper model will learn better and extract deeper features. Secondly, as the model becomes deeper, the computation load for the model training and model inference increases, which is indicated by the number of neurons and floating point operations (FLOPs). As the model will be deployed in the embedded system on the edge control units or the users' mobile phones, there is quite limited computation and memory storage in the microcontroller unit, especially for selected cost-effective STM32. Therefore, a trade-off between high accuracy and low model complexity is needed. Thirdly, as the model becomes deeper, the learning time becomes larger. For model 1, it takes approximately 150,000 epochs to converge, while it takes approximately 340,000 epochs to converge for model 4. Therefore, a trade-off between short learning time and high model complexity is needed.

TABLE I
Performance of Different Numbers of Layers in Autoencoders

Model Name	Model 1	Model 2	Model 3	Model 4
Model Structure	FC(30,16) FC(16,3) FC(3,16) FC(16,30)	FC(30,16) FC(16,12) FC(12,3) FC(3,12) FC(12,16) FC(16,30)	FC(30,16) FC(16,12) FC(12,8) FC(8,3) FC(3,8) FC(8,12) FC(12,16) FC(16,30)	FC(30,18) FC(18,16) FC(16,12) FC(12,8) FC(8,3) FC(3,8) FC(8,12) FC(12,16) FC(16,18) FC(18,30)
Number of Neurons	95	119	135	171
Number of Layers	4	6	8	10
FLOPs	**2632**	3544	4008	5688
RMSE	0.5184	0.4540	0.4437	**0.3956**

The performances of different dimensions of codings for autoencoders are summarized in Table II and Fig. 15. There are some interesting findings. Firstly, as the model becomes wider, that is codings dimensions are larger, the accuracy goes up. Secondly, the difference in accuracy increments is not large, but the computation load goes up. Hence, it is reasonable to determine codings dimensions of three, considering acceptable accuracy, high combability, and high interpretability (the latent ε, A, d spaces). Thirdly, learning curves for differently wide models are similar.

B. Decoder experimental results for flat surface pressure

The performance comparison among the decoder and conventional polynomial models is summarized in Table III. There are some intuitive findings. Firstly, it is observed that an increase in the order of polynomial models contributes to enhanced model accuracy. However, the optimal accuracy is achieved with the fourth-order polynomial model. Beyond this point, a further increase in the polynomial order results in diminished accuracy. This phenomenon can be attributed to the reason that polynomial models of higher orders become overfitted to the training dataset. Secondly, the accuracy of the MLP decoder outperforms all polynomial models, improving

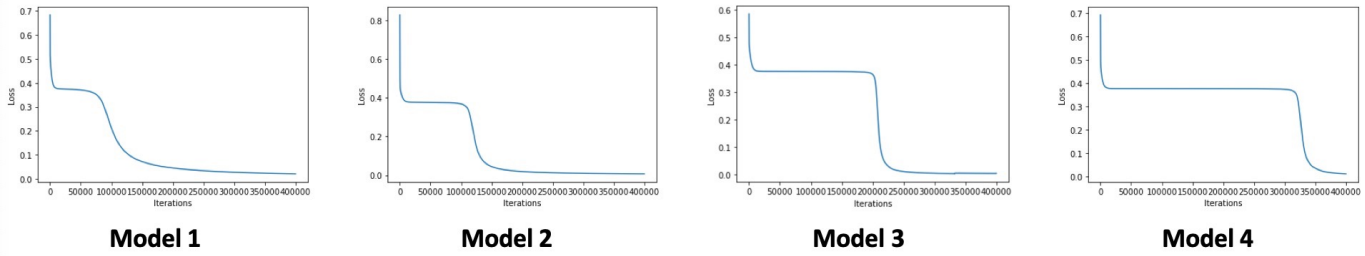

Fig. 14. Learning curves for different numbers of layers in autoencoders.

TABLE II
PERFORMANCE OF DIFFERENT DIMENSIONS OF CODINGS IN AUTOENCODERS

Model Name	Model a	Model b	Model c	Model d	Model e	Model f
Model Structure	FC(30,16) FC(16,1) FC(1,16) FC(16,30)	FC(30,16) FC(16,2) FC(2,16) FC(16,30)	FC(30,16) FC(16,3) FC(3,16) FC(16,30)	FC(30,16) FC(16,4) FC(4,16) FC(16,30)	FC(30,16) FC(16,5) FC(5,16) FC(16,30)	FC(30,16) FC(16,6) FC(6,16) FC(16,30)
Number of Neurons	93	94	95	96	97	98
Number of Codings Dimensions	1	2	3	4	5	6
FLOPs	**2488**	2560	2632	2704	2776	2848
RMSE	0.5191	0.5194	0.5184	0.5111	0.5104	**0.5078**

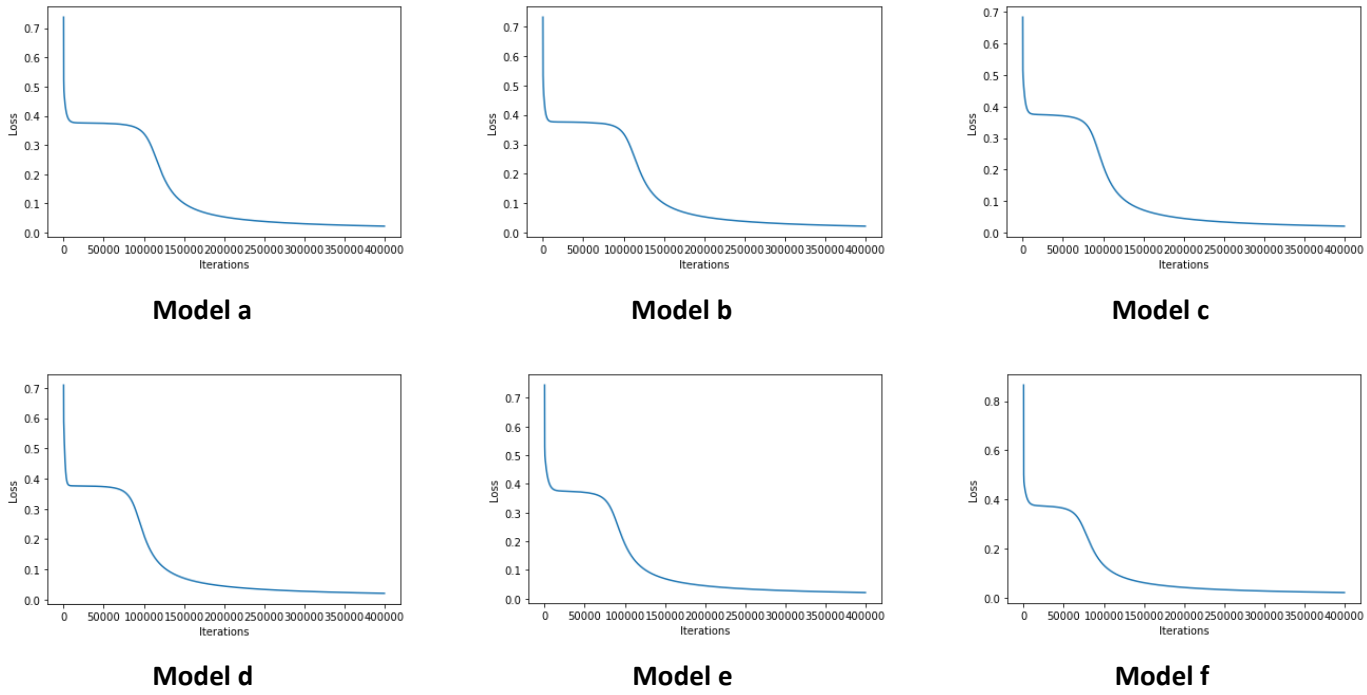

Fig. 15. Learning curves for different dimensions of codings in autoencoders.

accuracy by 38% compared with the best fourth-order polynomial model. Thirdly, the high accuracy of the neural network decoder is at the cost of higher model complexity, indicated by the total number of neurons and computation complexity of FLOPs.

The performances of the fine-tuning with a little computation load are summarized in Table IV. All the fine-tuned models' accuracies outperform the best of the polynomial models, which verifies that the trained decoder model is capable of generalization for different autoencoders and offers well parameters initialization which can largely cut down the fine-tuning relearning time.

TABLE III

PERFORMANCE OF THE PROPOSED DECODER MODEL AND POLYNOMIAL MODELS

Model Name	Encoder (autoencoder)	Decoder	Polynomial Degree 1	Polynomial Degree 2	Polynomial Degree 3	Polynomial Degree 4	Polynomial Degree 5
Model Structure	FC(30,18) FC(18,16) FC(16,12) FC(12,8) FC(8,3)	FC(3,8) FC(8,16) FC(16,32) FC(32,64) FC(64,64) FC(64,64) FC(64,1)	$y = ax + b$	$y = ax^2 + bx + c$	$y = ax^3 + bx^2 + cx + d$	$y = ax^4 + bx^3 + cx^2 + dx + e$	$y = ax^5 + bx^4 + cx^3 + dx^2 + ex + f$
Number of Neurons	87	252	2	3	4	5	6
FLOPs	24920		**2**	5	8	11	14
RMSE	**0.7891**		6.4231	1.895	1.8081	1.2754	1.9224

TABLE IV

PERFORMANCE OF DIFFERENT FINE-TUNING MODELS

Model Name	Encoder (Model 1) + Decoder	Encoder (Model 2) + Decoder	Encoder (Model 3) + Decoder	Encoder (Model 4) + Decoder	Polynomial Degree 4
Encoder Model Structure	FC(30,16) FC(16,3)	FC(30,16) FC(16,12) FC(12,3)	FC(30,16) FC(16,12) FC(12,8) FC(8,3)	FC(30,18) FC(18,16) FC(16,12) FC(12,8) FC(8,3)	
Decoder Model Structure	FC(3,8) FC(8,16) FC(16,32) FC(32,64) FC(64,64) FC(64,64) FC(64,1)	FC(3,8) FC(8,16) FC(16,32) FC(32,64) FC(64,64) FC(64,64) FC(64,1)	FC(3,8) FC(8,16) FC(16,32) FC(32,64) FC(64,64) FC(64,64) FC(64,1)	FC(3,8) FC(8,16) FC(16,32) FC(32,64) FC(64,64) FC(64,64) FC(64,1)	$y = ax^4 + bx^3 + cx^2 + dx + e$
Number of Neurons	298	310	318	336	5
FLOPs	23392	23848	24080	24920	**11**
RMSE	0.9266	0.9024	0.9149	**0.7891**	1.2754

C. Encoder-Decoder experimental results for curved surface pressure

The same encoder-decoder architecture with the same hyperparameters design was utilized for the curved surface pressure dataset. Hence, it is obtained a unified encoder and distinct decoders. The comparison between the proposed encoder-decoder models and conventional polynomial models are summarized in Table V, Table VI, Table VII, for positions B, B1, and C, respectively.

There are some intuitive findings. Firstly, it is observed that an increase in the order of polynomial models contributes to enhanced model accuracy. Nonetheless, the optimal accuracy is achieved with the third-order polynomial and the fourth-order polynomial model for the B1 position curve and the C position curve respectively. This observation can be attributed to the reason that polynomial models of higher orders are prone to overfitting the training dataset, thereby compromising their generalizability. Secondly, the accuracy of the encoder-decoder MLP model outperforms all polynomial models, improving accuracy by 98%, 97%, 98%, for the B position, B1 position, C position respectively. Thirdly, the high accuracy of the encoder-decoder MLP model is at the cost of higher model complexity, indicated by the total number of parameters and FLOPs. This trade-off highlights the need for careful consideration in the selection of models, balancing accuracy against computational efficiency.

D. Encoder-Decoder models frequency response analysis

To analyze the frequency response characteristics of linear components of trained models, the Dirac delta function was utilized as an input to the encoder-decoder MLP models for both flat and curved surface pressure. The models' output was subsequently transformed into the frequency domain by using the Fast Fourier Transform (FFT) to obtain the frequency response. Fig. 16 illustrates a comparison, demonstrating that all models significantly suppress all non-zero frequency components while substantially enhancing zero frequency components, akin to the behavior of low-pass filters.

E. Experimental results discussion

Firstly, based on previous experiments conducted on flat and various curved surfaces, it is evident that optimal polynomial methods are not linear equations. Specifically, a fourth-order polynomial model is optimal for flat surface pressure, a fifth-order polynomial model for the B position, a third-order polynomial for the B1 position, and a fourth-order polynomial model for the C position. Traditionally,

TABLE V

PERFORMANCE OF THE PROPOSED ENCODER-DECODER MODEL AND POLYNOMIAL MODELS ON B POSITION

Model Name	Encoder (autoencoder)	Decoder	Polynomial Degree 1	Polynomial Degree 2	Polynomial Degree 3	Polynomial Degree 4	Polynomial Degree 5
Model Structure	FC(30,18) FC(18,16) FC(16,12) FC(12,8) FC(8,3)	FC(3,8) FC(8,16) FC(16,32) FC(32,64) FC(64,64) FC(64,64) FC(64,1)	$y = ax + b$	$y = ax^2 + bx + c$	$y = ax^3 + bx^2 + cx + d$	$y = ax^4 + bx^3 + cx^2 + dx + e$	$y = ax^5 + bx^4 + cx^3 + dx^2 + ex + f$
Number of Neurons	87	252	2	3	4	5	6
FLOPs	24920		**2**	5	8	11	14
RMSE	**0.0283**		3.6445	1.3806	1.3508	1.3533	1.3464

TABLE VI

PERFORMANCE OF THE PROPOSED ENCODER-DECODER MODEL AND POLYNOMIAL MODELS ON B1 POSITION

Model Name	Encoder (autoencoder)	Decoder	Polynomial Degree 1	Polynomial Degree 2	Polynomial Degree 3	Polynomial Degree 4	Polynomial Degree 5
Model Structure	FC(30,18) FC(18,16) FC(16,12) FC(12,8) FC(8,3)	FC(3,8) FC(8,16) FC(16,32) FC(32,64) FC(64,64) FC(64,64) FC(64,1)	$y = ax + b$	$y = ax^2 + bx + c$	$y = ax^3 + bx^2 + cx + d$	$y = ax^4 + bx^3 + cx^2 + dx + e$	$y = ax^5 + bx^4 + cx^3 + dx^2 + ex + f$
Number of Neurons	87	252	2	3	4	5	6
FLOPs	24920		**2**	5	8	11	14
RMSE	**0.0633**		4.3389	1.9887	1.9342	1.9377	1.9386

TABLE VII

PERFORMANCE OF THE PROPOSED ENCODER-DECODER MODEL AND POLYNOMIAL MODELS ON C POSITION

Model Name	Encoder (autoencoder)	Decoder	Polynomial Degree 1	Polynomial Degree 2	Polynomial Degree 3	Polynomial Degree 4	Polynomial Degree 5
Model Structure	FC(30,18) FC(18,16) FC(16,12) FC(12,8) FC(8,3)	FC(3,8) FC(8,16) FC(16,32) FC(32,64) FC(64,64) FC(64,64) FC(64,1)	$y = ax + b$	$y = ax^2 + bx + c$	$y = ax^3 + bx^2 + cx + d$	$y = ax^4 + bx^3 + cx^2 + dx + e$	$y = ax^5 + bx^4 + cx^3 + dx^2 + ex + f$
Number of Neurons	87	252	2	3	4	5	6
FLOPs	24920		**2**	5	8	11	14
RMSE	**0.0387**		2.4482	1.5721	1.5568	1.5561	1.5563

capacitive sensors are understood to exhibit good linearity [12]–[14]. However, this study demonstrates that higher-order polynomial models provide a more accurate description, particularly when microstructures are incorporated into the dielectric layer to enhance sensor sensitivity. Secondly, the encoder–decoder MLP models introduced in this study are specifically designed for computational efficiency and lightweight implementation, making them highly suitable for deployment on resource-constrained edge control units. By leveraging temporal features within the sensor data, these models demonstrate a marked improvement over traditional polynomial regression methods, particularly in their ability to suppress noise. This advantage is critical given the viscoelastic properties of the textile sensors, which can introduce complex, time-dependent artifacts into pressure measurements. Thirdly, the encoder–decoder MLP models are both interpretable and physics-informed, as they explicitly incorporate the capacitance–pressure relationship into the learning process. Their unsupervised learning framework enables robust performance even in the presence of unknown or variable noise distributions, ensuring a high degree of generalizability. This agnostic learning capability was validated through extensive experimental evaluations, which confirmed consistent accuracy across both flat and curved surface pressure measurements. Fourthly, our investigation into model architecture revealed that deeper neural networks yield superior accuracy compared to wider configurations, although this comes with increased computational requirements. The encoder–decoder framework

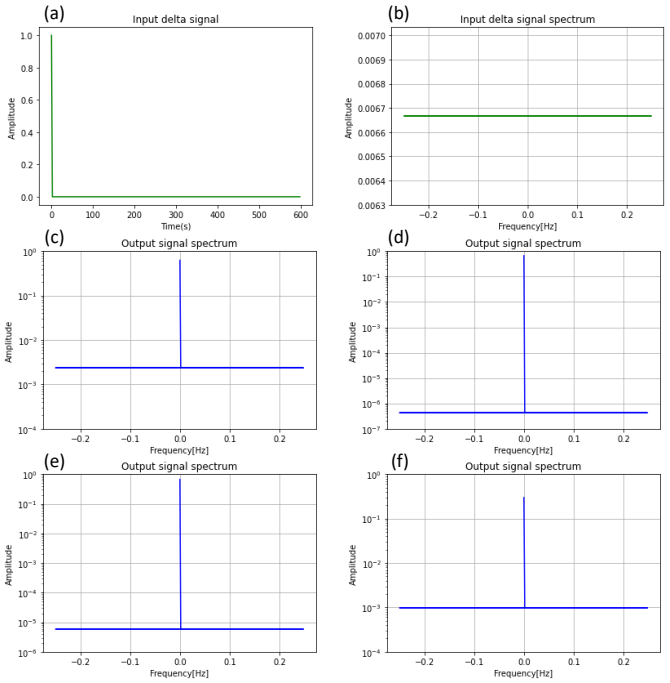

Fig. 16. Frequency responses of the linear components in trained encoder-decoder MLP models. Input Dirac delta function in the time domain (a) and frequency domain (b); Output frequency response for flat surface pressure (c), curved surface pressure at position B (d), curved surface pressure at position B1 (e), curved surface pressure at position C (f) respectively.

also supports efficient parameter initialization and fine-tuning, facilitating the interchangeability of encoders and promoting robust generalization across a variety of sensing conditions. Fifthly, the frequency responses of linear components of the encoder-decoder MLP models demonstrate suppression of all non-zero frequency components while enhancing zero frequency components. Consequently, the linear component of the learned encoder-decoder MLP model inherently acquired the desired low-pass filter characteristics to reduce noise in the designed static experiments.

F. Limitations and future work

This study introduces a unified encoder-decoder MLP architecture that demonstrates suitability for edge computation, high interpretability, and improved accuracy. Despite these advantages, several limitations remain that warrant further investigation and development.

Firstly, to enhance model interpretability, both flat and curved surface pressure datasets were collected under static pressure conditions, which are representative of slow movement scenarios. However, the model's performance under dynamic pressure conditions, such as those arising from rapid or complex movements, remains untested. These scenarios may exhibit different data distributions, potentially leading to reduced model accuracy. Future work should therefore include the collection and analysis of dynamic pressure data to ensure robust model generalization.

Secondly, to improve computational efficiency, the current approach segments one-minute time-series capacitance data for parallel processing by the MLP models. While this enables efficient computation, it may not fully capture temporal dependencies inherent in time-series data. Recurrent neural network architectures such as RNNs, LSTMs, and GRUs are well-suited for sequential data but typically require serial computation, which can be less efficient on edge devices. Further research is needed to systematically compare the trade-offs between parallelizable MLPs and sequential models in this context.

Thirdly, complex application situations may introduce dataset shift, potentially degrading model performance. Data augmentation techniques using generative models such as GANs, VAEs, diffusion models, or foundation models may help increase data diversity. However, ensuring that the generated data adhere to the underlying physical laws governing sensor behavior remains a significant challenge and requires further exploration.

Looking ahead, our future work will focus on improving sensor fabrication processes to enhance batch consistency. We plan to conduct experiments involving a cohort of human subjects to evaluate the performance of smart compression stockings embedded with the proposed models. Additionally, we aim to develop data augmentation methods that are constrained by physical laws to improve interpretability, controllability, and traceability. The next generation of edge control units will be designed with advanced accelerators such as GPUs and FPGAs, enabling the deployment of more computationally intensive algorithms. Finally, we intend to conduct long-term clinical trials to assess system performance and undertake comprehensive user experience and usability studies, as there exists a clear causal link in clinical practice: superior fit leads to improved comfort and compliance, which in turn enhances therapeutic efficacy.

V. Conclusion

In conclusion, this study advances the conservative management of chronic venous disease by introducing and validating a smart compression stocking system that integrates compression garments with embedded textile capacitive pressure sensors, a compact edge control unit, a dedicated mobile application, and advanced edge signal processing algorithms. The laboratory-fabricated sensors demonstrated high sensitivity, particularly in the clinically relevant low-pressure range below 50 mmHg, as well as satisfactory accuracy, repeatability, low energy consumption, and rapid response times. The edge control units, produced at a cost-effective price (US$33), further enhance the system's safety, portability, and sustainability, supporting the feasibility of large-scale deployment.

A central contribution of this work is the development of a unified encoder-decoder MLP architecture. The encoder, constructed using the symmetrical stacked autoencoder, enables effective nonlinear feature extraction and high-level abstraction, while the decoders are tailored for specific downstream tasks. This lightweight architecture is interpretable, physics-informed, and supports unsupervised learning, making it well-suited for deployment on resource-constrained edge devices.

Extensive empirical validation was performed using comprehensive datasets, which included 22,498 capaci-

tance–pressure data pairs collected from 100-minute recordings at each pressure level on flat surfaces, as well as 75,888 capacitance–pressure data pairs obtained from 12-minute recordings at each pressure level on curved surfaces over a ten-day period.

The proposed deep neural network algorithms were benchmarked against traditional polynomial regression methods. The results consistently demonstrated that the neural network models outperformed the benchmarks, achieving a RMSE of 0.7891 mmHg for flat surface pressure, a 38% improvement over polynomial regression. Fine-tuning with various encoder substitutions maintained robust performance, with RMSE values around 0.9 mmHg. For curved surface pressure measurements, the algorithms achieved RMSEs of 0.0283 mmHg, 0.0633 mmHg, and 0.0387 mmHg at positions B, B1, and C, respectively, corresponding to improvements of 98%, 97%, and 98% over traditional methods.

The findings of ablation studies further indicate that deeper neural networks provide superior accuracy compared to wider architectures, albeit with increased computational demands. The encoder-decoder framework also facilitates efficient parameter initialization and fine-tuning, supporting the interchangeability of encoders and robust generalization across diverse sensing scenarios. Notably, the linear components of the trained models exhibited low-pass filter characteristics, consistent with the empirical study design and effective for noise suppression.

Although the proposed algorithms require higher computational and storage resources, their substantial improvements in accuracy and generalization highlight the significant potential of the smart compression stocking system. Driven by the unified encoder-decoder MLP architecture, this system offers precise, real-time pressure monitoring and represents a promising advancement in the management of chronic venous disease.

REFERENCES

[1] J. Raffetto and F. Mannello, "Pathophysiology of chronic venous disease," *International angiology: a journal of the International Union of Angiology*, vol. 33, no. 3, pp. 212–221, 2014.

[2] R. T. Eberhardt and J. D. Raffetto, "Chronic venous insufficiency," *Circulation*, vol. 130, no. 4, pp. 333–346, 2014.

[3] J. Hill, G. Howatson, K. van Someren, S. Davidson, and C. Pedlar, "Pressures exerted by commercially available lower limb compression garments," *British Journal of Sports Medicine*, vol. 48, no. 7, pp. 608–608, 2014.

[4] F. Amsler and W. Blättler, "Compression therapy for occupational leg symptoms and chronic venous disorders–a meta-analysis of randomised controlled trials," *European Journal of Vascular and Endovascular Surgery*, vol. 35, no. 3, pp. 366–372, 2008.

[5] A. Belbasis, F. K. Fuss, and J. Sidhu, "Muscle activity analysis with a smart compression garment," *Procedia Engineering*, vol. 112, pp. 163–168, 2015.

[6] A. Belbasis and F. K. Fuss, "Development of next-generation compression apparel," *Procedia Technology*, vol. 20, pp. 85–90, 2015.

[7] A. Belbasis, F. K. Fuss, and J. Sidhu, "Estimation of cruciate ligament forces via smart compression garments," *Procedia Engineering*, vol. 112, pp. 169–174, 2015.

[8] A. Belbasis, "Muscle and soft tissue monitoring via smart compression garments," Thesis, RMIT University, 2021.

[9] B. Greenspan and M. A. Lobo, "Design and initial testing of an affordable and accessible smart compression garment to measure physical activity using conductive paint stretch sensors," *Multimodal Technologies and Interaction*, vol. 4, no. 3, p. 45, 2020.

[10] C. Gonçalves, A. F. da Silva, R. Simoes, J. Gomes, L. Stirling, and B. Holschuh, "Design and characterization of an active compression garment for the upper extremity," *IEEE/ASME Transactions on Mechatronics*, vol. 24, no. 4, pp. 1464–1472, 2019.

[11] C. Gonçalves, A. F. da Silva, and R. Simoes, "Wearable textile elongation sensor," in *Proc. 5th Int. Conf. Integrity Reliab.–Failure*, 2016, Conference Proceedings, pp. 90–95.

[12] S. T. Yang, J. W. Ryu, S.-H. Park, Y. B. Lee, S. H. Koo, Y.-L. Park, and G. Lee, "An active compression sleeve with variable pressure levels using a wire-fabric mechanism and a soft sensor," *Smart Materials and Structures*, vol. 28, no. 11, p. 114002, 2019.

[13] R. Qin, M. Hu, X. Li, T. Liang, H. Tan, J. Liu, and G. Shan, "A new strategy for the fabrication of a flexible and highly sensitive capacitive pressure sensor," *Microsystems & nanoengineering*, vol. 7, no. 1, p. 100, 2021.

[14] A. Atalay, V. Sanchez, O. Atalay, D. M. Vogt, F. Haufe, R. J. Wood, and C. J. Walsh, "Batch fabrication of customizable silicone-textile composite capacitive strain sensors for human motion tracking," *Advanced Materials Technologies*, vol. 2, no. 9, p. 1700136, 2017.

[15] A. Servati, L. Zou, Z. J. Wang, F. Ko, and P. Servati, "Novel flexible wearable sensor materials and signal processing for vital sign and human activity monitoring," *Sensors*, vol. 17, no. 7, p. 1622, 2017.

[16] K. T. Sweeney, T. E. Ward, and S. F. McLoone, "Artifact removal in physiological signals—practices and possibilities," *IEEE transactions on information technology in biomedicine*, vol. 16, no. 3, pp. 488–500, 2012.

[17] T. Tamura, Y. Maeda, M. Sekine, and M. Yoshida, "Wearable photoplethysmographic sensors—past and present," *Electronics*, vol. 3, no. 2, pp. 282–302, 2014.

[18] P. Celka, R. Vetter, P. Renevey, C. Verjus, V. Neuman, J. Luprano, J.-D. Decotignie, and C. Piguet, "Wearable biosensing: signal processing and communication architectures issues," *Journal of Telecommunications and Information Technology*, pp. 90–104, 2005.

[19] R. Yousefi, M. Nourani, S. Ostadabbas, and I. Panahi, "A motion-tolerant adaptive algorithm for wearable photoplethysmographic biosensors," *IEEE journal of biomedical and health informatics*, vol. 18, no. 2, pp. 670–681, 2013.

[20] S. H. Kim, D. W. Ryoo, and C. Bae, "Adaptive noise cancellation using accelerometers for the ppg signal from forehead," in *2007 29th Annual International Conference of the IEEE Engineering in Medicine and Biology Society*. IEEE, 2007, Conference Proceedings, pp. 2564–2567.

[21] M. Raghuram, K. V. Madhav, E. H. Krishna, N. R. Komalla, K. Sivani, and K. A. Reddy, "Dual-tree complex wavelet transform for motion artifact reduction of ppg signals," in *2012 IEEE international symposium on medical measurements and applications proceedings*. IEEE, 2012, Conference Proceedings, pp. 1–4.

[22] W. Navaraj and R. Dahiya, "Fingerprint-enhanced capacitive-piezoelectric flexible sensing skin to discriminate static and dynamic tactile stimuli," *Advanced Intelligent Systems*, vol. 1, no. 7, p. 1900051, 2019.

[23] Y. Wang, X. Wu, D. Mei, L. Zhu, and J. Chen, "Flexible tactile sensor array for distributed tactile sensing and slip detection in robotic hand grasping," *Sensors and Actuators A: Physical*, vol. 297, p. 111512, 2019.

[24] L. Zou, X. Chen, A. Servati, S. Soltanian, P. Servati, and Z. J. Wang, "A blind source separation framework for monitoring heart beat rate using nanofiber-based strain sensors," *IEEE Sensors Journal*, vol. 16, no. 3, pp. 762–772, 2015.

[25] Q. Wang, P. Yang, and Y. Zhang, "Artifact reduction based on empirical mode decomposition (emd) in photoplethysmography for pulse rate detection," in *2010 Annual International Conference of the IEEE Engineering in Medicine and Biology*. IEEE, 2010, Conference Proceedings, pp. 959–962.

[26] "Medical compression hosiery—quality assurance ral-gz 387/1," 2008.

[27] I. Swain, *The measurement of interface pressure*. Springer, 2005, pp. 51–71.

[28] H. Luo, Y. Xiong, M. Zhu, X. Wei, and X. Tao, "Integrated wearable system for monitoring skeletal muscle force of lower extremities," *Sensors (Basel, Switzerland)*, vol. 24, no. 14, 2024.

[29] A. Zhang, Z. C. Lipton, M. Li, and A. J. Smola, "Dive into deep learning," *arXiv preprint arXiv:2106.11342*, 2021.

[30] K. Hornik, M. Stinchcombe, and H. White, "Multilayer feedforward networks are universal approximators," *Neural networks*, vol. 2, no. 5, pp. 359–366, 1989.

[31] Q. Xu, Y. Shi, J. Bamber, Y. Tuo, R. Ludwig, and X. X. Zhu, "Physics-aware machine learning revolutionizes scientific paradigm for machine learning and process-based hydrology," *arXiv preprint arXiv:2310.05227*, 2023.